ORIGINAL ARTICLE

Characterization of Tin Disulfide Thin Films Prepared by Spin Coating Technique: Effect of Spin Speed and Deposition Time on Film Properties

Kazi Hanium Maria[1] · **Rezaul Md. Kabir**[1] · **I. N. Esha**[1] · **F. T. Z. Toma**[2] · **M. S. Bashar**[3] · **Kazi Md. Amjad Hussain**[2]

Abstract Thin films of SnS_2 were synthesized by spin coating technique at room temperature using an aqueous solution of stannic chloride and thioacetamide as the absorber layer in solar cells. The films were deposited at different spin speeds and spin times, and their effect on the properties of the thin films was studied. The spin speed was varied from 1000 to 2000 rpm, and the spin time was from 60 to 120 s for each speed. The structure of the films was found to be face-centered cubic with preferential orientation along the (002) plane; there was no sign of other unwanted phases. With increasing spin speeds and deposition times, the crystallinity of the sample was improved for a certain speed, after that, it deteriorated crystallinity. FTIR peaks confirmed the presence of Sn–S bonds in all the prepared films. Morphological results of the films were consisting of small spherical grains in an aggregated form that is abated by spin speed. EDAX revealed that the thin film was found near stoichiometric and some excess amount of tin was present in the sample. Atomic force microscopy showed the presence of grains, hills, and valleys on the surfaces of thin films. XPS results confirmed the presence of Sn and S in the deposited films. The band gap values for the films deposited at 1500 rpm for 90 s calculated from the absorbance spectra increased from 2.9 to 3.5 eV with an increase in deposition time attributed to a change in film thickness.

1 Introduction

Environmentalists prefer to adopt domestic sustainable energy sources for the future of renewable energy. Therefore, much attention is required to prepare high-efficiency solar cells from copious and innocuous materials at a low cost [1–3]. In that line, tin disulfide (SnS_2) could be considered an appropriate contender for solar cell devices including sensors, batteries, optoelectronics applications, biomedical science, and other multifunctional devices [4–8]. Tin disulfide (SnS_2) from binary chalcogenides compounds of IV–VI groups has a useful band gap (2.2–2.4 eV) in the visible range [9–12]. Two layers of sulfur atoms fold the thin atomic Sn layer by covalent interactions and form the hexagonal crystal arrangement [9]. As SnS_2 has a layered type of structure and layers are piling up with one another using van der Waals forces, it possesses a high absorption coefficient and potential [10, 11]. Based on the mole concentration of tin and sulfur, SnS_2 demonstrates both p-type and n-type conduction [11]. Tin sulfide can be assembled with multiple phases, such as SnS, SnS_2, Sn_2S_3, and Sn_3S_4, and tin and sulfur have different bonding characteristics [12, 13]. Among all the phases, SnS_2 thin films are one of the most stable phases of Sn–S from the application point of view.

A number of techniques such as atmospheric pressure chemical vapor deposition (APCVD) [14, 15], plasma-enhanced chemical vapor transport (PE-CVD) [16, 17], successive ionic layer adsorption and reaction (SILAR) [18], chemical bath deposition [19, 20], dip coating [2, 21], vacuum evaporation [22], chemical spray pyrolysis [23, 24], and spin coating [25–27] have been used for the preparation

✉ Kazi Hanium Maria
kazimaria@du.ac.bd

[1] Department of Physics, University of Dhaka, Dhaka 1000, Bangladesh

[2] Experimental Physics Division, Atomic Energy Centre, Dhaka 1000, Bangladesh

[3] Bangladesh Council of Scientific and Industrial Research (BCSIR), Dhaka 1205, Bangladesh

of SnS$_2$ thin films. In chemical vapor deposition (CVD), the thin film is deposited on a substrate at an elevated temperature by decomposing gases that contain the required chemical components [14, 15]. It can be carried out at low temperatures when the gases are transformed into a plasma state named plasma-enhanced chemical vapor deposition (PE-CVD) [14]. Atmospheric pressure chemical vapor deposition (AP-CVD) methods have used the precursor under vapor form and control the substrate temperature. This different CVD process generates film with uniform thickness and controlled porosity and little waste. The drawback of this method is the low deposition rate and high cost due to maintaining vacuum systems [16, 17]. The SILAR method comprises sequential reactions including the absorption and reaction of ions (anions and cations from solutions) and the rinsing process (deionized water) to prevent precipitation at the substrate solution interface for the deposition of thin films [18]. This complex method needs expensive autoclaves and affects the growth mechanism of films. Moreover, high pressure is produced at elevated temperatures during the reaction. The chemical bath deposition (CBD) method regulates the release of required metal cations and anions in an aqueous solution by using a suitable complex agent. The released cations and anions react to form compounds and deposit film on the substrates which are immersed in the solution [19, 20]. In dip coating methods, the wet liquid film is deposited on the substrate by dipping the substrate for a fixed time in a precursor solution and then pulling up the substrate vertically at a constant speed. The volatile solvent will be evaporated from the liquid by drying at room temperature, resulting in a thin film of coating on the substrate surface [2, 21]. Vacuum evaporation heats the solid material to evaporate inside the high vacuum chamber to form a thin film by adhering to the substrate [22]. On the other hand, chemical spray pyrolysis employs the atomization of chemical precursors into aerosol droplets that are sprayed on a hot substrate throughout a gas medium [23, 24]. All these techniques possess a few advantages and drawbacks as well as hold a few integral parameters such as substrate structure, operating temperature, vacuum condition, rate of deposition, and source which should be controlled precisely to deposit desired quality thin film. Compared to other methods, the spin coating technique can produce uniform, well-adherent thin film and is effective for large-area deposition. Being a facile and time-convenient process, the spin coating technique does not need a high reaction temperature or any special type of reactor and metal catalyst, making it accordant with advanced technology [25, 26]. Moreover, the process is compatible with flexible organic substrates and easy to scale up [27]. However, the film thickness and other properties depend on the nature of the solution like viscosity, surface tension, drying rate, the concentration of the solution, and the parameters selected for the spin process. Thereafter, two

crucial parameters, the spin speed and the deposition time, should be controlled and adjusted to improve the efficiency of the thin films. Therefore, spinning is required to spread the mixture over the substrate and continue to spin off the fluid at the edges of the substrate to achieve the desired film thickness. Therefore, the thin film's desired thickness and required properties cannot be obtained by excess spin speed and rampant spin duration. As mentioned above, this technique has already been used for the preparation of SnS$_2$ thin films [25–27]. In spite of such studies, an elaborative study is required to elect the suitable spin rotation and deposition time for the deposition of high-quality SnS$_2$ thin films with less thickness for better absorption in solar cell application. From our previous study, SnS$_2$ bulk powder was prepared by using SnCl$_4 \cdot$5H$_2$O and thioacetamide (C$_2$H$_5$NS) as the starting materials, and a solution of these two powders with distilled water was prepared with optimized centration [28]. The usage of that solution precursor might be appropriate for spin-deposited thin films. Therefore, this study has aimed at equipping SnS$_2$ thin films prepared by varying spin speed and deposition time to get adequate knowledge for better film deposition with less thickness. Eventually, the films' structural, morphological, and optical properties were investigated thoroughly to study the effect of spin speed and deposition time on films.

2 Materials and Methods

To prepare SnS$_2$ thin film by spin coating technique, stannic chloride pentahydrate (SnCl$_4$.5H$_2$O), thioacetamide (C$_2$H$_5$NS) powders, and concentrated hydrochloric acid (HCl 35% pure A.R.) were used from Sigma-Aldrich purchased. The solution was prepared by vigorously mixing 10 ml of 2.5 M stannic chloride pentahydrate with 48 ml of deionized water in a 100-ml dry glass beaker for 20 min. Then 2 ml of 2.5 M aqueous solutions of hydrochloric acid was added under continuous stirring to dissipate SnCl$_4$.5H$_2$O into water. After a while (~ 5 min), 0.3 g (4 mmol) of thioacetamide (C$_2$H$_5$NS) was added and the bath was stirred for 5 h. The pH of the solution was controlled at 2 (acidic) throughout the mixing of all chemicals. Finally, the solution was kept aging for 12 h. The solution turned to light yellow after aging and appeared as a dense type of solution at the bottom of the beaker. The upper one-third of the watery light solution was thrown out, and the dense yellow solution was collected and again blended with distilled water. The aging-decant-water add procedure was conducted three times to remove the excess amount of HCL. Then the final homogeneous solution was taken to prepare film by spin coating technique. The silica glass slide substrates were ultrasonically cleaned in ethanol and then dried in an oven for 1 h at 40 °C. This pre-cleaned glass slide was placed on the

substrate holder of the spin coating instrument, and 5 drops (~ 5 ml) of prepared SnS_2 solution were dropped on the glass slide using a pipette. Then the film was deposited by rotating the glass slide at 1000, 1500, and 2000 rpm for three different deposition times (60, 90, and 120 s) by spin coating instruments. The deposited films were annealed at 100 °C for 1 h before carrying out different characterizations. The experimental process is given schematically in Fig. 1.

The structural identification of the prepared SnS_2 films was investigated by the Philips X-pert pro-X-ray diffraction system with a filter for CuK_α irradiation at $\lambda = 1.5406$ Å. The thickness of the SnS_2 thin films was measured using a reflectometry-based thin-film measurement device (TF-166) at the experimental Physics Division of the Atomic Energy Commission, Dhaka (AECD). It is capable of measurement error < 1 nm or $\pm 0.5\%$ of the film thickness. This instrument is the most cost-effective solution for measuring films from 20 nm to 50 μm in thickness. Spectroscopic reflectometry measurement was involved in this technique. The thin-film surface was illuminated normally or at a certain angle with a tungsten halogen light. The film thicknesses were observed through spectral reflectance curve fitting. The surface morphology and topography of the film were thoroughly checked by the field-emission scanning electron microscopy (FESEM, ULTRA 55, Carl Zeiss AG) and atomic force microscope (AFM, Bruker, Dimension Icon). X-ray photoelectron spectroscopy (XPS, ULVAC-PHI 5000) with an Al K_α X-ray source (1486.6 eV) typically set at 3 kV, 24 W, and an angle of 45° was utilized to study the chemical state of the films. Optical transmittance and absorbance of the films were checked at room temperature in the range of 300–1200 nm with a Cary 5000- UV–Vis–NIR spectrophotometer. The thickness of the film was measured by the Fizeau fringe method, based on the principle of multiple beam interferometry.

3 Results and Discussion

3.1 Growth Mechanism

A comprehensive analysis should be carried out to determine the growth mechanism of SnS_2 formation. Based on our observation during the experiment and previous report [29], SnS_2 formation has been influenced by the production of S^{2-} ions in the different solvents. In this work, stannic ions initially form a complex by interacting with HCl acid, whereas the thioacetamide decomposition generates H_2S at room temperature which further decomposes to produce S^{2-} ion. Here, HCl was used to expedite the dissociation of thioacetamide to release H_2S gas [28, 30]. Finally, S^{2-} ion reacts with the Sn^{4+} ion and produces SnS_2. Two drops of HCl controlled the pH of the solution during the reaction. Later, excess HCl acid was removed by washing the solution with distilled water.

From the above discussion, the film deposition may involve the following chemical reaction wherein the conventional solution is produced and coats the substrate.
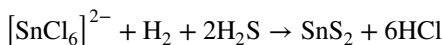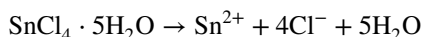
$$SnCl_4 \cdot 5H_2O \rightarrow Sn^{2+} + 4Cl^- + 5H_2O$$

$$Sn^{2+} + 4Cl^- + 2HCl \rightarrow \left[SnCl_6\right]^{2-} + H_2$$

$$C_2H_5NS + 2H_2O \rightarrow CH_3COOH + H_2S + NH_3$$

$$\left[SnCl_6\right]^{2-} + H_2 + 2H_2S \rightarrow SnS_2 + 6HCl$$

Figure 2a shows the XRD pattern of SnS_2 films deposited by different spin rotations keeping deposition time constant at 90 s, and the XRD pattern of the films deposited by varying deposition times at 1500 rpm is shown in
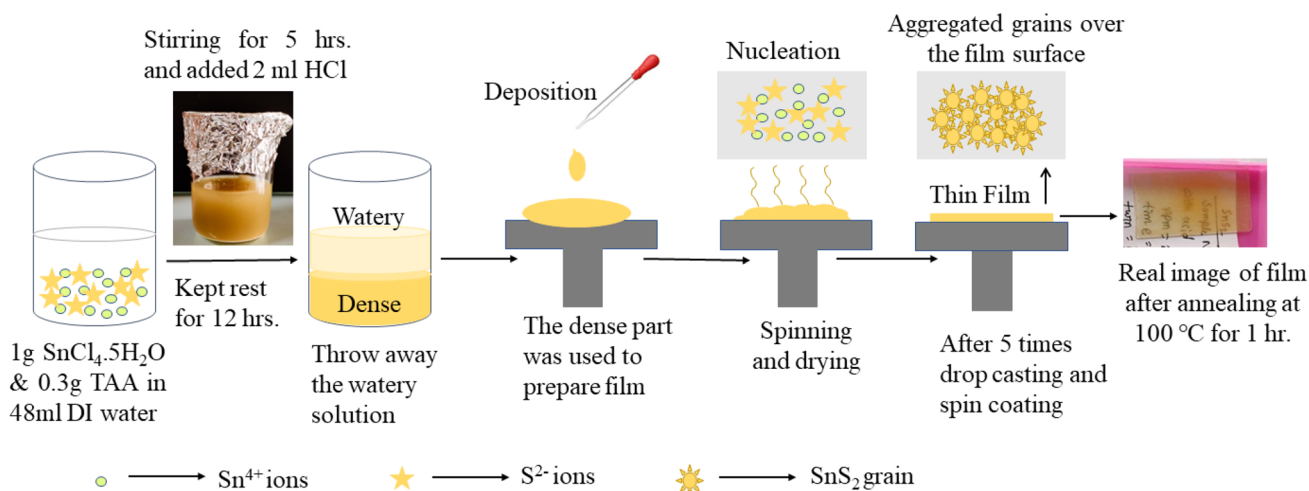

Fig. 1 Schematic illustrating the formation of SnS_2 thin films by spin coating

Fig. 2b. From Fig. 2a, it is evident that a more intense peak has appeared at the spin speed of 1500 rpm for a deposition time of 90 s. According to the patterns, the peak with 100% intensity appear at around 31.94° corresponding to reflection from the (002) crystallographic planes (JCPDS card No. 23-0677) of hexagonal phases [25]. This sharp peak confirms the good crystallinity of the tin disulfide thin films which contain only the pure SnS_2 phase [28, 31]. The c value of the lattice parameter of this 100% intensity peak is around 5.46 nm, and the value of the c/a ratio for other low intense peaks of the film deposited for 60 and 120 s is 1.51 which is also lower than the standard value of 1.61, JCPDS Card No. 23-0677 ($a = b = 3.648$ Å and $c = 5.899$ Å) [25]. It is seen that the spin speed and deposition time have a great influence on the film formation process and the film's crystallinity. At 1000 rpm for 60 s, the thick porous, and tacky-free film is seen to form, showing no intense peaks. When the spin speed is increased, it increases the centrifugal force which deposits thin, gluey, and quality thin films. However, the longer duration of the high centrifugal force might oust a large amount of solution from the substrate and deposit less amount of solution, inhibiting the film's crystallization [25]. The average crystallite size is calculated only for the film deposited at 1500 rpm for 90 s, because the single peak ranging from 31.24° to 32.66° of two theta appears as the most intense and obvious peak in the diffraction pattern. The average crystallite size for 90 s has been figured out around 12.82 nm with a small dislocation density around 0.0060 nm^{-2} using modified Debye Scherrer's formula [32] and uniform deformation model [32]. This large grain size and small dislocation density demonstrate the better crystallization of the film deposited at 1500 rpm for 90 s.

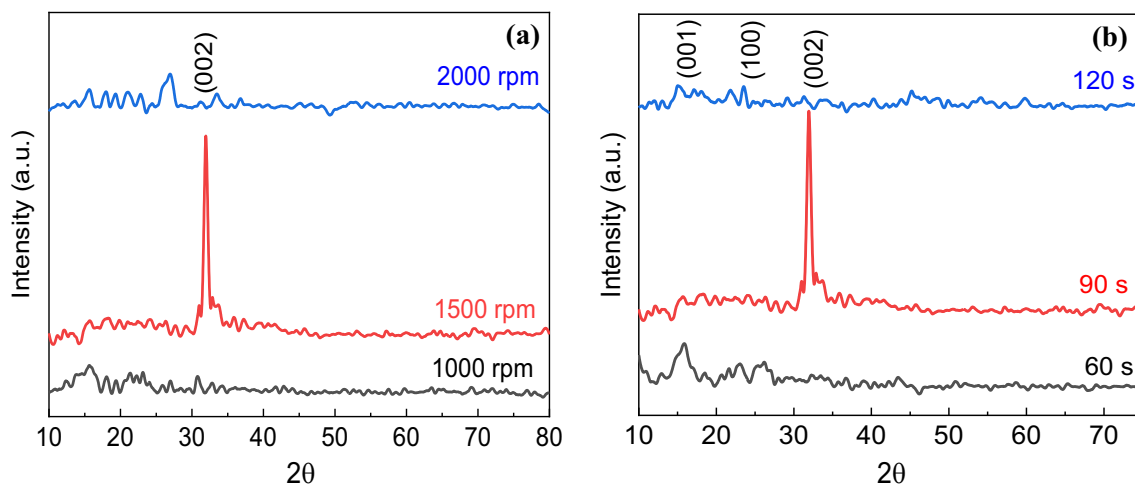The slight variation in film thickness is observed with the increase of spin speed (rpm) and spin time as shown in Fig. 3. Increased rpm increases the centrifugal force on the solution as well as on the substrate which casts away surplus solution and allows less solution for thin-film formation on the substrate. As a result, the film thickness decreases [25]. It is for this same reason that a long duration of deposition time deposits less thick films. The deposition was carried out at least three times for each spin speed and deposition time to prove the reproducibility of the film with the same thickness. Here, the variation in film thickness with the spin speed and time is found insignificant. However, the film thickness follows the inverse proportional law with spin speed and spin time. Generally, a large variation of spin speed (rpm) around a factor of ten changes the film thickness, and minor speed variation results slight change in thickness. The film
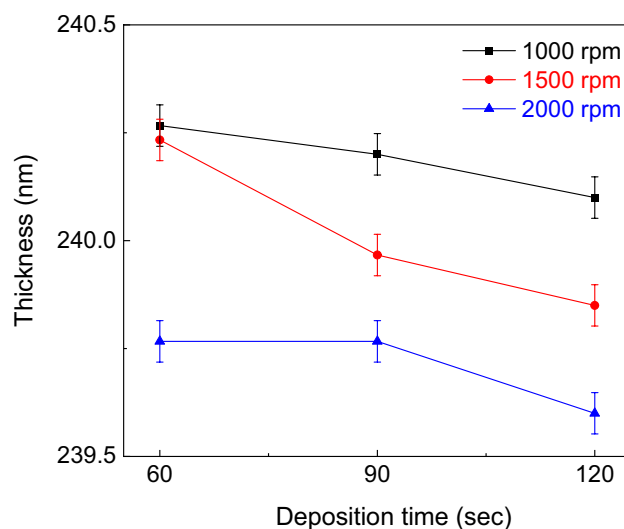

Fig. 3 Deposition time versus thickness of SnS_2 thin films at different spin speeds

Fig. 2 X-ray diffraction patterns of SnS_2 thin film with **a** 90-s deposition time for 1000, 1500, 2000 rpm deposition rate and **b** 60-s, 90-s, 120-s deposition time for 1500 rpm deposition rate

thickness also depends on the concentration of the material dissolved in the solvent. Therefore, the film thickness is assumed to be changed in a narrow range with these spin speeds for a chosen concentration of SnS_2 solution.

Figure 4a shows the Fourier transform infrared (FTIR) spectroscopy of the spin coating deposited SnS_2 thin films for three deposition spin rotations of 1000, 1500, and 2000 rpm for a constant deposition time of 90 s. FTIR spectra were also taken for three different deposition times of 60, 90, and 120 s in the same deposition spin speed of 1500 rpm as shown in Fig. 4b. In both cases, broadband is observed at 3429.6 cm^{-1} in every spectrum which is the vibration mode of O–H groups specifying the absorption of water by the surface [33]. The spectra also show the strong C–H stretching band at 2919.6 cm^{-1} due to moisture and CO_2 absorption in the SnS_2 films. The peak at 2378.6 cm^{-1} is assigned to the stretching vibration of Sn–S bonds which illustrates the formation of SnS_2 films. Two bands are observed at 1224.4 cm^{-1} and 1627.4 cm^{-1}, corresponding to bond vibrations of C–O and C–H that probably come from thioacetamide [33]. The broad band at 1082.4 cm^{-1} indicates the stretching vibration of the C–O–C bond. The Sn–S bond vibrations are evident from the band at 489.6 cm^{-1} [33]. FTIR analysis results strongly confirm the presence of bonding between Sn and S atoms in the as-prepared samples and also show consistency with XRD results.

The SEM micrograph surface image of the SnS_2 thin films synthesized by the spin coating technique for different deposition times and different spin speeds is shown in Fig. 5a–i. The growth mechanism, shape, and size of particles are clearly understood from the image. The image reveals that the deposited thin film covers the complete surface of the substrate. A compact and dense homogenous surface is observed in all the samples which contain a large number of small grains in aggregated form. The film deposited for 60 s at three different spin speeds (Fig. 5a–c) shows an even surface consisting of small spherical grain. The film deposited for 90 s (Fig. 5d–f) demonstrates a rough surface stuffed with a slightly abate grain size than that of the film deposited for 60 s. The films that were deposited for 120 s (Fig. 5g–i) at different spin speeds present a much rougher surface with a lack of grain growth as crystallization decreases for high spin speed and longer duration. The enhanced surface roughness with increased spin speed is attributed to a decrease in grain size, surface defect, and some sort of strain that arises during growth. The observed decrease in grain size implies the degradation in crystal quality which is also confirmed by the XRD result. From the SEM image, the grain size is measured by the distance between the visible grain boundaries which is larger than the grain size measured from XRD peaks. Because the XRD method calculates the crystalline development, which directs to a smaller grain size [34].

Compositional analysis of the film deposited at 1500 rpm for three different deposition times was carried out by using the EDAX technique to study the stoichiometry of the film. The EDAX spectrum of the SnS_2 thin film was recorded in the binding energy region of 0.0–14 eV as shown in Fig. 6a–c, and the variation of the Sn to S atomic ratio was calculated from the figure. The chemical composition of the deposited SnS_2 thin film was detected to be near-stoichiometry ratio with slightly Sn-rich. The S content was noticed to slightly decrease with the increase of the deposition time. The S deficiency can be related to the slow dissociation of thioacetamide in the solution [28].

Images of atomic force microscope from SnS_2 thin films deposited at the spin speed of 1500 rpm for 90 s are
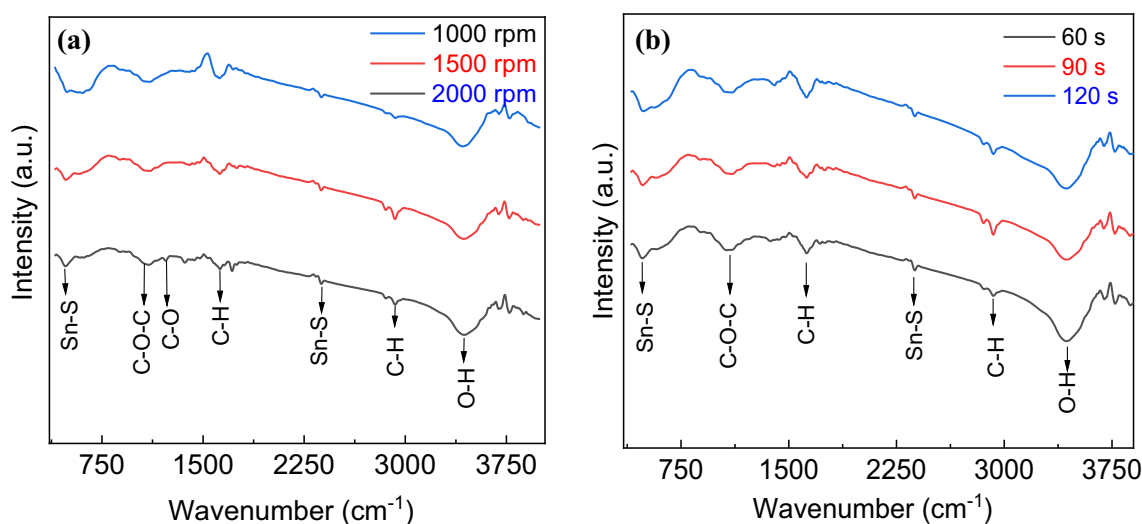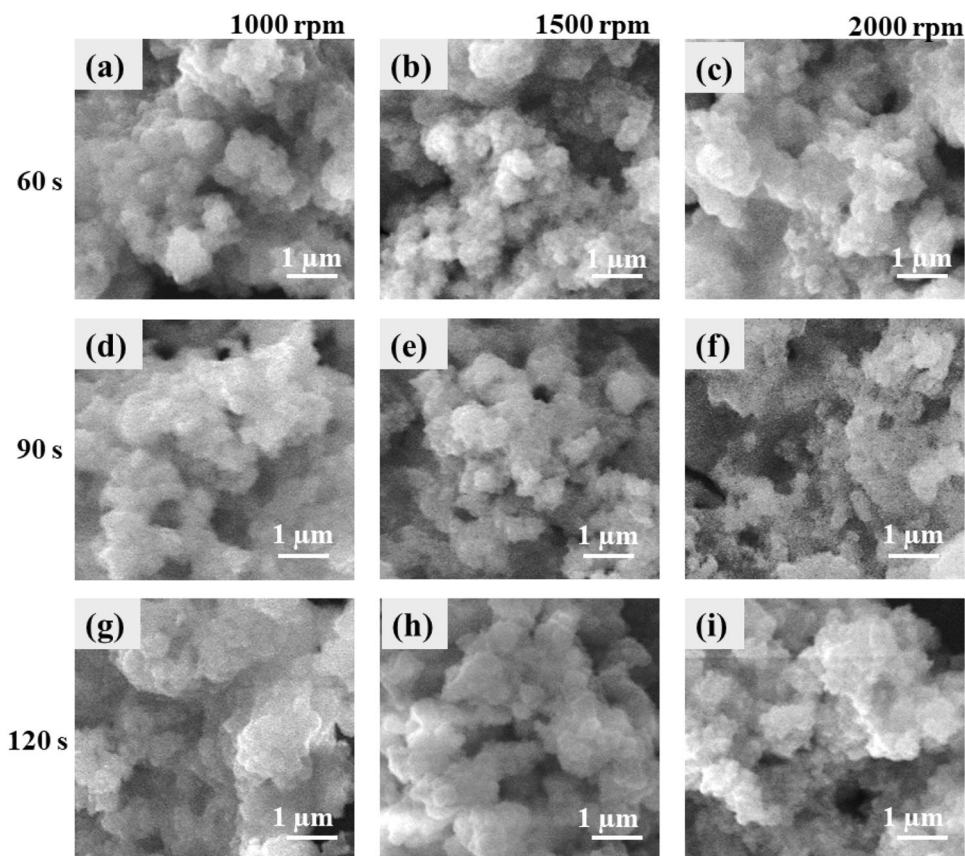

Fig. 4 FTIR spectra of SnS_2 thin films for **a** 90-s deposition time with 1000, 1500, 2000 rpm deposition rate and **b** 60 s, 90 s, 120 s deposition times with 1500 rpm deposition rate

Fig. 5 SEM image of SnS₂ thin films deposited at three different deposition speeds (1000, 1500, 2000 rpm) for three different deposition times (60 s, 90 s, 120 s)

illustrated in Fig. 7. The AFM profiles show high roughness of the samples of about 85 mm. Many hills and valleys have appeared throughout the observed region, indicating the presence of well-segregated grains which is consistent with the XRD result.

To elucidate the chemical state, valence band position, and binding energy of the SnS₂ thin films, XPS was performed in the range of 0–1250 eV with the films prepared at 1500 rpm for 90 s, and the survey spectrum is shown in Fig. 8a. The XPS survey reveals the presence of Sn, S, Cl, C, N, and O elements indicating the successful formation of the SnS₂ film. The peak detected at 285.03 eV is assumed to be adventitious carbon C 1s which may have originated from the surface contamination. The O 1s signal at 531.49 eV may appear as a constituent of the glass substrate or could have arisen from the metal oxide. The Cl 2p (199.39 eV) and N 1s (401.07 eV) peaks might have resulted from the ambient contamination and absorbed impurities from HCl and thioacetamide.

Figure 8b shows the high-resolution XPS spectra of the Sn 3d peaks of SnS₂ film deposited at 1500 rpm for three different deposition times. The Sn 3d spectrum exhibits spin-orbital double peaks of Sn 3d5/2 and Sn 3d3/2 indicating the pure Sn. The binding energy (BE) peaks are observed for Sn 3d5/2 and Sn 3d3/2 at 487.38 and 495.78 eV, respectively,

for the deposition time of 90 s. From the graph, it is clearly seen that the binding energy of the Sn 3d orbitals shifts to lower binding energies and becomes slightly broader without a change of the spectral shape for the deposition time of 60 s and 120 s. This binding energy shift might relate to the oppressed chemical valence of Sn at the position of sulfur vacancies which reveals the weak formation of SnS₂ lattice. However, the spin–orbit splitting between the two peaks remains at 8.40 eV for all the deposition times, which confirms that Sn is in the Sn⁴⁺ state [35]. Besides, the spectra of Sn 3p1, Sn 3p3, and Sn 3s are also found at 706.25 eV, 757.50 eV, and 888.75 eV, respectively, in the full survey of the SnS₂ film (Fig. 8a).

The S 2p high-resolution region spectrum is shown in Fig. 8c. The binding energy for S 2p 3/2 is noticed at around 161.78 eV due to S²⁻ ions for the film deposited at 1500 rpm for three different deposition times. The low intense and diffused S 2p3/2 peak is observed for the deposition time of 60 s and 120 s which indicates a lower stoichiometry and deficient formation of the SnS₂ phases in both cases. In the case of the deposition time of 90 s, S 2p exhibits two distinct peaks with binding energies of 161.6 and 162.9 eV are attributed to S 2p3/2 and S 2p1/2. These two peaks confirm the metal–sulfur bonding which is caused by the spin–orbit coupling of S²⁻ in SnS₂. Besides, the deformation of S 2p1/2
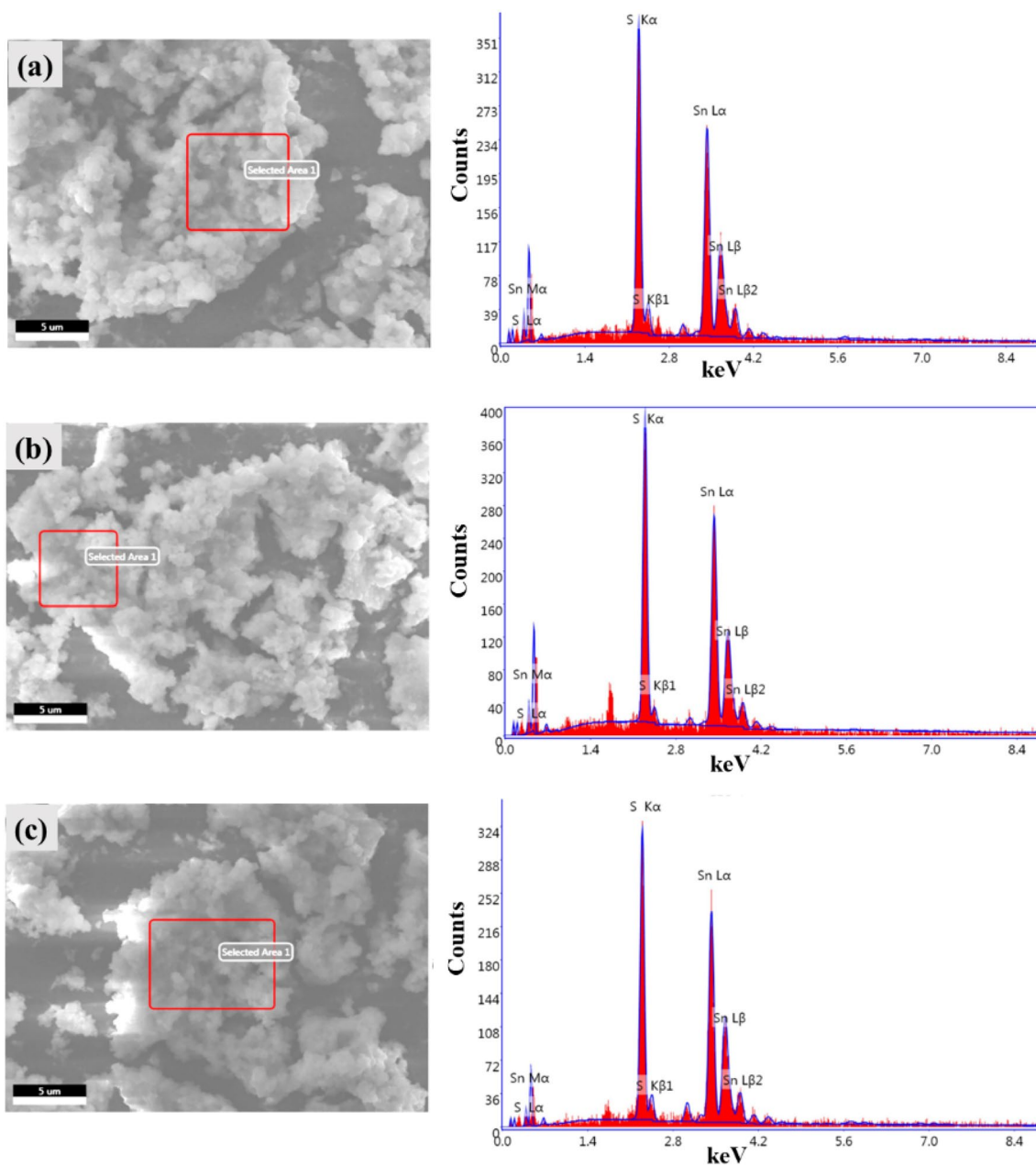
Fig. 6 EDAX spectrum of SnS$_2$ thin films deposited at 1500 rpm for three different deposition times (60 s, 90 s, 120 s)

indicates a smaller amount of S in the films [28]. The value of the molar ratio Sn/S (1:1.52) calculated from the quantity of Sn and S from the XPS peak area (Sn 3*d* and S 2*p*) for the deposition time of 90 s indicates the Sn-rich SnS$_2$ film formation. This result is consistent with the values reported in the EDAX results [28, 35].

Figure 9a, b shows UV–VIS transmittance and absorbance spectra of SnS$_2$ thin films deposited at a constant spin speed of 1500 rpm for different deposition times in the 300–800 nm wavelength range. The transmittance of all the deposited films decreases in visible and near-infrared ranges,

increasing with the deposition time from 60 to 120 s. Above 396 nm, a plateau has appeared with an increase in wavelength though the value remains less than 40% transparent for 90 and 120 s in mentioned wavelength range, while the maximum transparency observed for the 60 s is around 50% as shown in Fig. 9a. This decrease in the transmittance with the deposition time shows the increase in absorbance for that particular number of times.

Figure 9b shows that the optical absorptions of the films are found to increase from 290 nm with increasing wavelength, reach its edge, and then start to decrease with the
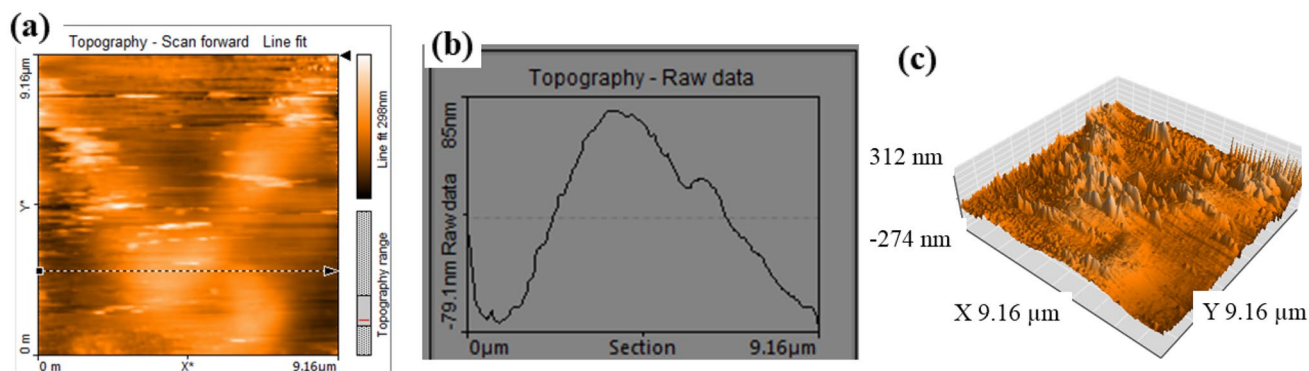
Fig. 7 AFM images of the surface and profiles of SnS_2 thin film deposited at 1500 rpm for 90 s
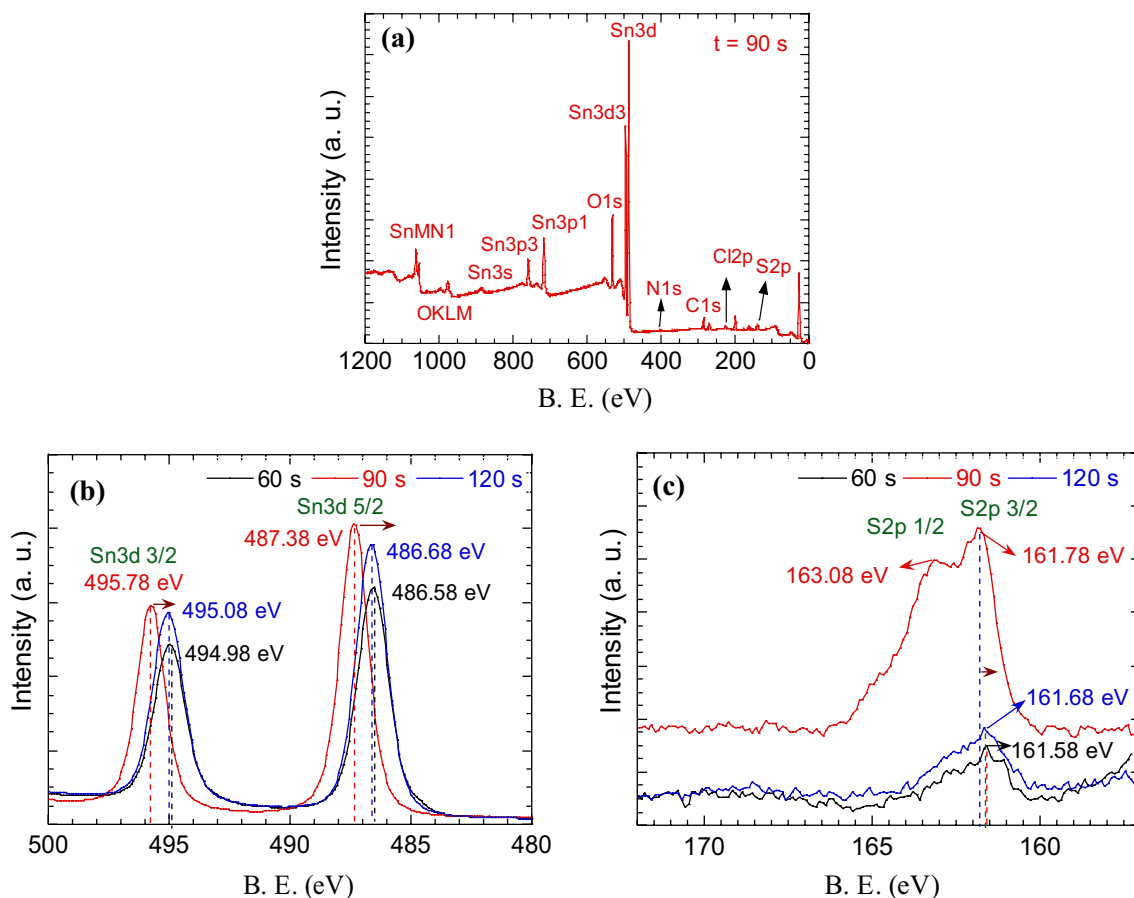

Fig. 8 **a** XPS survey of SnS_2 thin film deposited at 1500 rpm for 90 s. **b** Variation of XPS spectra for Sn 3d region and **c** S 2p region of the films deposited at 1500 rpm for different deposition times

wavelength. This sharp decrease in the absorption at a certain wavelength implies the presence of an optical band gap in the samples. In addition, the absorbance edge is noticed to shift slightly towards a longer wavelength with the increase of deposition time, indicating the variation in film thickness. The optical band gap of SnS_2 thin film is calculated from the absorbance spectra using Tauc's formula [36]. The

films are found to exhibit both direct and indirect bandgap, and the values are listed in Table 1. Figure 10a, b demonstrates that both direct and indirect bandgap are decreasing with the deposition time for the film deposited at 1500 rpm. Generally, the shortening of the energy band gap is linked with large crystalline size and impurity concentration. Large crystallites enclose a higher number of atoms and atomic
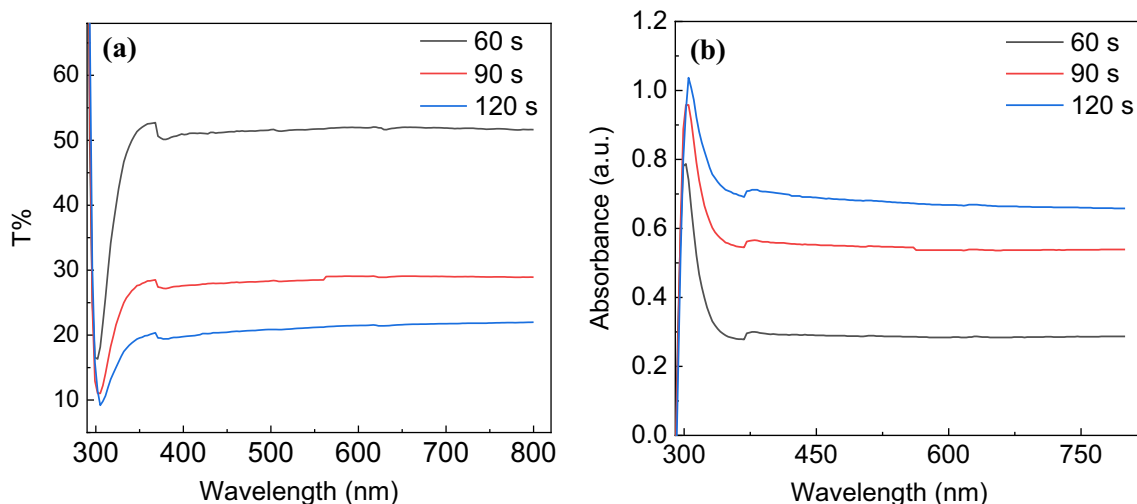
Fig. 9 Variation of **a** transmittance and **b** absorbance of SnS$_2$ thin films deposited at 1500 rpm for different deposition times

orbital which escalates the bonding and antibonding effect. As a result, the gap between the valence and conduction band decreases. In addition, the reduction of the bandgap is strongly dependent upon the impurity band developed by the overlapped impurity states. Therefore, synthesis methods and conditions should be taken care of to limit the contamination in the deposited film.

The variation of band gap with different deposition times at three spin speeds is presented in Fig. 11a–c. In the case of 1000, the widening of the band gap with deposition time might be associated with the accession of crystallinity in the films as evident in the SEM image. In this case, the energy level reduces with the decrease in grain size, creating a larger gap between the valence and conduction bands. The

SEM image also shows that the film deposited at 2000 rpm has irregular grain growth with deposition time which might affect the band gap. Chaki *et al.* spin-coated SnS$_2$ thin films at different deposition times of 2 s, 4 s, and 6 s and reported an increasing trend in direct band gap value from 2.36 to 2.44 eV and indirect band gap value from 1.32 to 1.40 eV [25, 37]. In this work, the band gap value is obtained more than the band gap of bulk SnS$_2$, as prepared SnS$_2$ is nano-structured and exhibits weak crystallinity owing to more strains and dislocation [38].

The effect of spin speed and deposition time on the properties of our thin film has been compared with other SnS$_2$ thin films deposited by spin coating with different parameters which are presented in Table 1. Compared to

Table 1 A comparative study of SnS$_2$ thin films deposited by spin coating with this work

| Deposition time (s)	Spin speed (rpm)	Band gap, Eg (eV)	Grain size (μm)	Film thickness (nm)	Transmittance (T%)	References
2	1000	Direct (2.44–2.36)		7110	***	25
4	1500			3910		
6	2000	Indirect (1.40–1.32)		2480		
30	1500	2.46 ± 0.05		50–48	***	27
60	2500			30–28		
	3500			25–23		
30	2000	2.54	0.6	300–600	~60%	39
		2.25	0.3			
30	1500	2.24		***	***	40
900	10,000	2.8		50	***	41
60	1000	Direct (3.85–3.65)	0.71–0.51	240.3–240.1	Less than 40%	This work
90	1500		0.79–0.5	240.2–239.9		
120	2000	Indirect (3.43–2.27)	0.91–1.0	239.8–239.6		

* = no measure values
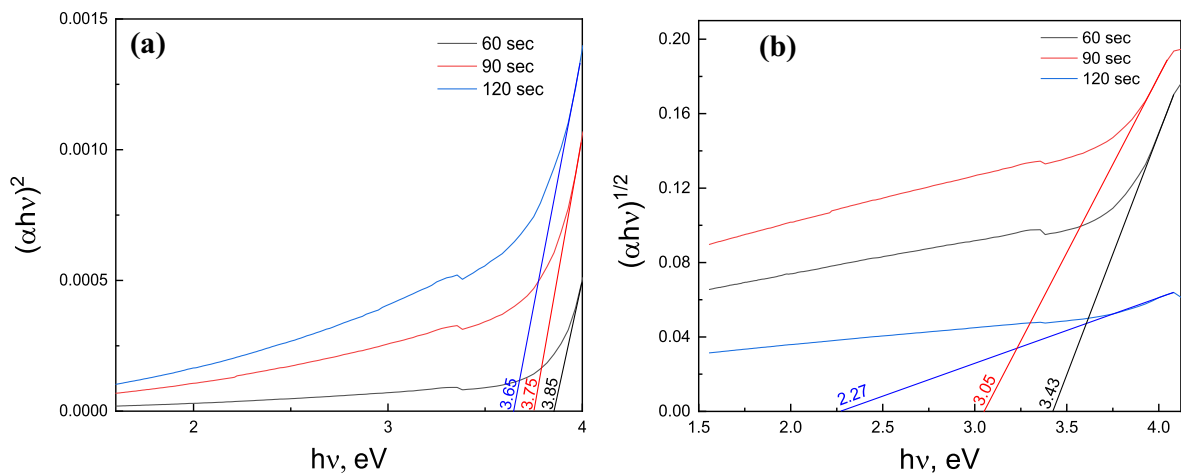
Fig. 10 a Direct band gap and **b** indirect band gap of SnS$_2$ thin films deposited at 1500 rpm for different deposition times
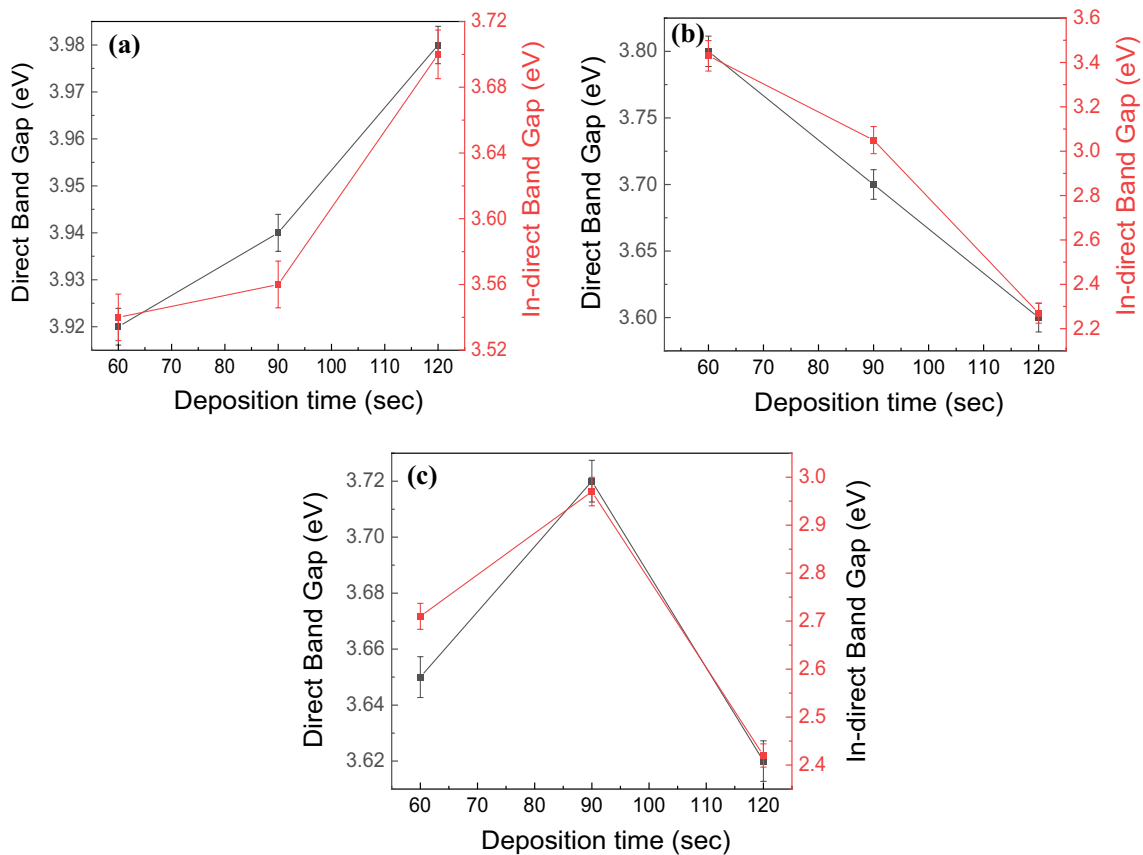

Fig. 11 Variation of direct band gap and indirect band gap with deposition time of SnS$_2$ thin films deposited at **a** 1000, **b** 1500, **c** 2000 rpm

others research [25, 27, 39–41], our prepared films exhibit a wider bandgap and higher reflectance which can be used to operate at higher temperatures. Furthermore, decreased and controlled film thicknesses have been obtained with the same speed but longer deposition. However, it paves the way

for further optimization of deposition parameters, including exploring other experimental parameters like growth temperature and deposition time to build one film layer over another. Table 1 also exhibits that the spin-coated SnS$_2$ thin film deposited at 1500 rpm for 90 s is less transmissive and

has a wide band gap. These properties may be useful for preparing the solar collector's mirror in solar cell applications (Fig. 11).

4 Conclusion

This work concluded that the spin speed and time influenced the SnS_2 thin film having large grain and wide band gap. Consequently, a comprehensive study of the structural and optical properties of SnS_2 thin films was performed by varying spin speed and deposition time. It was established from the XRD pattern that the predominant growth plane of the tin disulfide films was (002). The structural analysis results indicated that spherically shaped particles of different sizes were distributed randomly over the surface of the films. The films deposited for higher spin speed and longer deposition time had better crystallinity than those deposited for shorter times. The best crystallinity of SnS_2 was obtained at 1500 rpm for 90 s. FTIR spectra of SnS_2 films proved the formation of Sn–S bonds for all the deposition speeds and times. The 3D AFM analysis showed hills and valleys features. The optical studies revealed that the transmittance of all layers was lower than 40% in the visible region, demonstrating that 1500 rpm was the optimum spin speed at the point of optical properties in the SnS_2 thin film. The achieved results are deliberated in detail which is very important for many applications in the industry.

Authors Contributions KHM helped in conceptualization, supervision, writing—original draft preparation, reviewing and editing. RMK was involved in investigation, methodology, reviewing. INE contributed to investigation, writing—original draft preparation, reviewing and editing. FTZT performed investigation, methodology. MSB and KMAH investigated the study.

Data Availability The data supporting this study's findings are available from the corresponding author upon reasonable request.

Declarations

Conflict of interest The authors declare no competing interest. Only the authors had the right to publish the results as they were involved in the design of the study; in the collection, analyses or interpretation of data; in the writing of the manuscript.

Human and Animal Rights This article does not contain any studies with human participants or animals performed by the author.

References

1. Voznyi A, Kosyak V, Opanasyuk A S, Tirkusova N, Grase L, Medvids A, and Mezinskis G, *Mater Chem Phys* **173** (2016) 52. https://doi.org/10.1016/j.matchemphys.2016.01.036
2. Panda S K, Antonakos A, Liarokapis E, Bhattacharya S, and Chaudhuri S, *Mater Res Bull* **42** (2007) 576. https://doi.org/10.1016/j.materresbull.2006.06.028
3. Tan F, Qu S, Wu J, Liu K, Zhou S, and Wang Z, *Nanoscale Res Lett* **6** (2011) 298. https://doi.org/10.1186/1556-276X-6-298
4. Zeng Y, Li W, Zhang H, Wu X, Sun W, Zhu Z, and Yu Y, *Anal Methods* **6** (2014) 404. https://doi.org/10.1039/C3AY41644E
5. Su G, Hadjive V G, Loya P E, Zang J, Lei S, Maharjan S, Dong P, Ajayan P M, Lou J, and Peng H, *Nano Lett* **15** (2015) 506. https://doi.org/10.1021/nl503857r
6. Du N, Wu X, Zhai C, Zhang H, and Yang D, *J. Alloys Compd* **580** (2013) 457. https://doi.org/10.1016/j.jallcom.2013.06.079
7. Shi W, Huo L, Wang H, Zhang H, Yang J, and Wei P, *Nanotechnology* **17** (2006) 2981. https://doi.org/10.1088/0957-4484/17/12/016
8. Chaki S H, Deshpande M P, Trivedi D P, Tailor J P, Chaudhary M D, and Mahato K, *Appl Nanosci* **3** (2013) 189. https://doi.org/10.1007/s13204-012-0123-7
9. Huang Y, Sutter E, Sadowski J T, Cotlet M, Monti O L A, and Racke D A, *ACS Nano* **8** (2014) 10743. https://doi.org/10.1021/nn504481rC2014
10. Nakashima S, Katahama H, and Mitsuishi A, *Phys B+C* **105** (1981) 343. https://doi.org/10.1016/0378-4363(81)90272-2
11. Abass A K, Jassim H A, Majeid K J, and Misho R H, *Phys Status Solidi* **91** (1985) 129. https://doi.org/10.1016/0038-1098(86)90180-8
12. Burton L A, Colombara D, Abellon R D, Grozema F C, Peter L M, and Savenije T J, *Chem Mater* **25** (2013) 4908. https://doi.org/10.1021/cm403046m
13. Kherchachi I B, Attaf A, and Saidi H, *Main Group Chem* **15** (2016) 231. https://doi.org/10.3233/MGC-160202
14. Hibbert T G, Mahon M F, Molloy K C, Price L S, and Parkin P, *J Mater Chem* **11** (2001) 469. https://doi.org/10.1039/B005863G
15. Price L S, Parkin I P, Hardy A M E, and Clark R J H, *Chem Mater* **11** (1999) 1792. https://doi.org/10.1021/cm990005z
16. Wang S, Wang S, Chen J, Liu P, Chen M, and Xiong H, *J Nanoparticle Res* **16** (2014) 2610. https://doi.org/10.1007/s11051-014-2610-0
17. Juarez A S, Silver A T, and Ortiz A, *Thin Solid Films* **480** (2005) 452. https://doi.org/10.1016/j.tsf.2004.11.012
18. Deshpande N G, Sagade A A, Gudage Y G, Lokhande C D, and Sharma R, *J Alloys Compd* **436** (2007) 421. https://doi.org/10.1016/j.jallcom.2006.12.108
19. Reddy K T R, Sreedevi G, and Wilson M P, *Mater Sci Eng A* **3** (2013) 182.
20. Reddy K T R, Sreedevi G, Ramya K, and Miles R W, *Energy Proc* **15** (2012) 340. https://doi.org/10.1016/j.egypro.2012.02.041
21. Ray S C, Karanjai M K, and Gupta D D, *Thin Solid Films* **350** (1999) 72. https://doi.org/10.1016/S0040-6090(99)00276-X
22. Shi C, Chen Z, Shi G, Sun R, Zhan X, and Shen X, *Thin Solid Films* **520** (2012) 4898. https://doi.org/10.1016/j.tsf.2012.03.050

23. Thangaraju B, and Kaliannan P, *J Phys D Appl Phys* **33** (2000) 1054. https://doi.org/10.1088/0022-3727/33/9/304

24. Jaber A Y, Alamri S N, and Aida M S, *J Appl Phys* **51** (2012) 065801. https://doi.org/10.1143/JJAP.51.065801

25. Chaki S H, Joshi H J, Tailor J P, and Deshpande M P, *Mater Res Express* **4** (2017) 076402. https://doi.org/10.1088/2053-1591/aa72b6

26. Mitzi D B, Kosbar L L, Murray C E, Copel M, and Afzali A, *Nature* **428** (2004) 299. https://doi.org/10.1038/nature02389

27. Řičica T, Střižík L, Dostál L, Bouška M, Vlček M, Beneš L, Wágner T, and Jambor R, *Appl Organomet Chem* **29** (2015) 176. https://doi.org/10.1002/aoc.3267

28. Maria K H, Sakhuja N, Jha R K, and Bhat N, *IEEE Sens J* **21** (2021) 10420. https://doi.org/10.1109/JSEN.2021.3059087

29. Khimani A J, Chaki S H, Chauhan S M, and Deshpande M P, *J Mater Sci Mater Electron* **30** (2019) 13118. https://doi.org/10.1007/s10854-019-01675-5

30. Butler E A, Peters D G, and Swift E H, *Anal Chem* **30** (1958) 1379. https://doi.org/10.1021/ac60140a027

31. Niu L, Li K, Zhen H, Chui Y S, Zhang W, Yan F, and Zheng Z, *Small* **10** (2014) 4651. https://doi.org/10.1002/smll.201401647

32. Yadav S, Singh M, Verma D K, and Gautam J, *Adv Nano Energy* **1** (2017) 73.

33. Mariappan R, Ragavendar M, and Ponnuswamy V, *Opt Appl* **4** (2011) 989.

34. He K, Chen N, Wang C, Wei L, and Chen J, *Cryst Res Technol* **53** (2018) 170015. https://doi.org/10.1002/crat.201700157

35. Yuan Y J, Chen D Q, Shi X F, Tu J R, Hu B, Yang L X, Yu Z T, and Zou Z G, *Chem Eng J* **313** (2017) 1438. https://doi.org/10.1016/j.cej.2016.11.049

36. Chaki S H, Deshpande M P, and Tailor J P, *Thin Solid Films* **550** (2014) 291. https://doi.org/10.1016/j.tsf.2013.11.037

37. Domingo G, Iroga R S, and Kanneswurf C R, *Phys Rev* **143** (1966) 536. https://doi.org/10.1103/PhysRev.143.536

38. Xia C, Zhao X, Peng Y, Zhang H, Wei S, and Jia Y, *Superlattices Microstruct* **85** (2015) 664. https://doi.org/10.1016/j.spmi.2015.05.050

39. Orletskyi I G, Solovan M M, Maryanchuk P D, Maistruk E V, Pinna F, Tresso E, and Brus V V, 10612, (2018). https://ui.adsabs.harvard.edu/link_gateway/2018SPIE10612E.0PO. https://doi.org/10.1117/12.23 03838

40. Rajwar B K, and Sharma S K, *Opt Quantum Electron* **54** (2022) 72. https://doi.org/10.1007/s11082-021-03424-7

41. Gedi S, Alhammadi S, Noh J, Reddy V, Reddy M, Park H, Rabie A M, Shim J J, Kang D, and Kim W K, *Nanomaterials* **12** (2022) 282. https://doi.org/10.3390/nano12020282